A high-order harmonic generation apparatus for time- and angle-resolved photoelectron spectroscopy

B. Frietsch,[1] R. Carley,[1,2] K. Döbrich,[2] C. Gahl,[1] M. Teichmann,[1] O. Schwarzkopf,[3] Ph. Wernet,[3] and M. Weinelt[1, a)]

[1)] *Freie Universität Berlin, Arnimallee 14, 14195 Berlin, Germany*

[2)] *Max-Born-Institut, Max-Born-Str. 2a, 12489 Berlin, Germany*

[3)] *Helmholtz-Zentrum Berlin für Materialien und Energie GmbH, Albert-Einstein-Str. 15, 12489 Berlin, Germany*

(Dated: 18 June 2013)

We present a table top setup for time- and angle-resolved photoelectron spectroscopy (tr-ARPES) to investigate band structure dynamics of correlated materials driven far from equilibrium by femtosecond laser pulse excitation. With the electron-phonon equilibration time being in the order of one to two picoseconds it is necessary to achieve sub-picosecond time resolution. Few techniques provide both the necessary time and energy resolution to map non-equilibrium states of the band structure. Laser-driven high-order harmonic generation is such a technique. In our experiment a grating monochromator delivers tunable photon energies up to 40 eV. A photon energy bandwidth of 150 meV and a pulse duration of 100 fs FWHM allow us to cover the k-space necessary to map valence bands at different k_z and detect outer core states.

PACS numbers: 79.60.-i, 78.47.-p, 42.65.Ky

[a)] Corresponding author: weinelt@physik.fu-berlin.de

A. Motivation

Photoemission spectroscopy has proven to be a powerful tool for the investigation of electronic properties of solids. It has greatly developed, starting in the 1960s from binding energy measurements in normal emission to high resolution full k-space measurements with third generation synchrotron sources (see Ref. 1 and references therein). A big step in this development was the commercial availability of angle-resolving hemispherical analyzers. With full knowledge of the energetic band structure it was possible to examine quasi-particle interactions through their kink-like signatures in the band dispersion near the Fermi level.[2,3] At the same time spin detectors were combined with energy and angular resolution to obtain knowledge of exchange-split band structures and Fermi surfaces.[4–6] With this full set of measured quantities one important piece of information left is the dynamical behavior of the solid upon perturbation,[7,8] which is especially interesting for correlated materials such as ferromagnets,[9] superconductors,[10] charge-density-wave systems,[11] topological insulators,[12] or heavy fermion systems.[13] To cover quasi-particle interactions in the time domain it is desirable to operate on the sub-picosecond timescale. In recent years this challenge has been tackled by several complementary methods including measurements with free electron lasers sources,[14] femtosecond beam slicing with conventional synchrotron sources,[15–18] and the "table top" approach using a femtosecond laser-based monochromatized high-order harmonic light source, as presented in this paper.[19–23]

When near-IR laser intensities reach $10^{14}\,\mathrm{Wcm^{-2}}$ in rare gases, high-order harmonics of the laser frequency are generated. High-order harmonic generation (HHG) was first observed in the early 1990s and can be understood in a simple 3-step process.[24] In the first step, the electric field of the laser suppresses the atomic Coulomb potential, allowing a bound electron to tunnel into the continuum. The electron is then accelerated by the laser field and returns to the vicinity of its parent ion when the field reverses. Finally the electron recombines with the ion, releasing an extreme ultraviolet (XUV) photon with an energy that is an odd multiple of the IR photon energy. The probability of this recombination is of order 10^{-6} so the XUV photon yield is low and losses have to be minimized.

With the increasing availability of reliable femtosecond lasers, HHG has developed into a versatile source of XUV radiation. In addition, high-order harmonic radiation retains many desirable properties of the laser used to generate it. For use as a spectroscopic light source,

the most important of these are the spatial and temporal coherence, which lead respectively to the formation of a collimated beam of femtosecond XUV pulses.

Most high-order harmonic generation experiments are used for their femtosecond time resolution to investigate electron dynamics in atoms and molecules in the gas phase.[25] In contrast only a few experiments have been optimized for the investigation of dynamics in solids,[26,27] and only some of those look at transient band structures.[20,28–31] Our objective is to combine the power of ARPES with the fs time resolution and extreme-ultraviolet (XUV) photon energies available through HHG, the latter allowing access to high electron momenta to probe the whole Brillouin zone. Photoelectrons generated at these photon energies have mean free paths in the material of only a few Ångstrom, so this technique is inherently surface sensitive and probes the first few sub-surface layers to yield information on the bulk band-structure. Since the native bandwidth of even a single harmonic generated by a 40 fs near infrared laser pulse is on the order of $0.25 - 0.5\,\mathrm{eV}$,[32] it is desirable to select a fraction of the bandwidth. To this end we have designed and built a monochromator beamline delivering a bandwidth as small as 90 meV at 35.6 eV, while maintaining an overall time resolution better than 150 fs and sufficient photon flux for reasonable measurement times.

Apparatuses for time-resolved photoemission studies at surfaces have been presented by several authors with distinct objectives. The main differences between the setups are the repetition rate of the laser and the photon-energy selection, which is the primary focus of this paper. Currently there are several different approaches for wavelength selection, most common are single grating[19,23,32] and double grating[29,33,34] monochromators. Generally single grating arrangements have a higher transmission while double grating arrangements deliver shorter pulses by compensating the tilt of the wave front incurred by diffraction from a single grating. Both approaches can be modified to make use of conical diffraction to achieve higher transmission.[21,35] An alternative approach is to employ multilayer mirrors whose coating is tailored to reflect a fixed single harmonic from the frequency comb delivered in HHG,[30,36,37] or to select a broad bandwith close to the high-energy cutoff for attosecond spectroscopy.[28]

B. Beamline Design

Our approach seeks a compromise between energy and time resolution, while maintaining flexibility (i.e. wavelength tuneability), a high optical throughput and reduced optical com-

plexity. We therefore opted for a design based on a single-grating monochromator, with the grating mounted conventionally. Since the overall energy resolution of a monochromator is partially determined by the convolution of the input and output slits, it is desirable to have a mirror between the XUV source and the entrance slit of the monochromator to focus the XUV on the entrance slit. Otherwise the HHG source is effectively the entrance slit, and increasing the resolution by reducing its size (by making the IR focus smaller) may have undesirable consequences for HHG efficiency. Therefore we included a mirror before and after the monochromator. To obtain a high reflectivity, the mirrors and grating are designed for grazing incidence and are therefore toroidal. Our design also makes use of extensive differential pumping along the length of the beamline. From 10^{-3} mbar at the HHG source, a pressure of better than $3 \cdot 10^{-11}$ mbar can be maintained indefinitely in the photoemission chamber, allowing for long measurement times without sample degradation.

To reach the desired performance, the optical design was optimized by modeling and ray tracing. The results are shown in Fig. 1. An overview of the apparatus is depicted in Fig. 2. The overall efficiency of the beamline was obtained with the REFLEC code,[38] taking into account the incidence angles and the micro-roughness of the optical surfaces, as well as the specified shape of the grating profile (Fig. 1). Geometrical effects (e.g., losses at the slits) and the transmission of the IR filtering aluminium foil are not included. An efficiency of 10 % or better could be achieved over the whole energy range. Starting with a 1.5 mJ IR pulse ($\hbar\nu = 1.5\,\mathrm{eV}$) at a pulse repetition rate of 10 kHz we obtain 10^{10} to 10^{11} photons/s in a single harmonic. The spot size at the sample position has a FWHM diameter of about 130 $\mu\mathrm{m}^2$.

Simulations using the RAY code[39] yielded the spectral and temporal widths of the transmitted harmonic pulses as shown in Fig. 1 (b) and (c). They where obtained by end-to-end simulations of trajectories originating from a model of the HHG source. The spectral width in Fig. 1 (b) includes both the monochromator band pass and the inherent spectral width of the respective harmonic, which was assumed to have a Lorentzian profile with a width of 250meV (for all harmonics up to order 39), as estimated from the width of photoelectron lines obtained with our HHG setup at Helmholtz-Zentrum Berlin.[40] For the 51^{st} order, a width of 420 meV was assumed.[41] These considerations demanded the inclusion of two exchangeable gratings to reach the desired energy resolution across the whole expected HHG spectrum. The low energy grating (LEG) for photon energies $15 - 40$ eV has 200 lines/mm. The high

energy grating for $35 - 110\,\mathrm{eV}$ photons has 500 lines/mm. For slit openings $\geq 100\,\mu\mathrm{m}$, the monochromator acts more or less as a harmonic filter, i.e. the complete selected harmonic is transmitted and maximum flux is achieved. Reducing the slit size yields better energy resolution, at the price of lower photon flux.

The calculated temporal pulse broadening of the harmonic by the grating is shown in Fig. 1 (c). As the temporal broadening is mainly determined by the number of illuminated grooves of the grating, i.e., the tilt of the wave front, it depends both on the divergence of the incoming harmonic beam and the angle of incidence on the grating. Therefore the broadening is energy (i.e. harmonic order) dependent, but for all harmonics lies in the range of $100 - 150$ fs according to our ray tracing.

An analytic expression for the pulse broadening may be found in Ref. 42. To first order pulse broadening stems from the lateral dispersion and is determined by the available bandwidth at each point of the exit slit, i.e., the energy resolution of the monochromator grating $\Delta\lambda = N \cdot \lambda$, where N is the number of illuminated lines. For illustration we calculate the temporal broadening at 35.6 eV due to the LEG. The monochromator entrance arm is 331 mm long so, assuming a divergence of the harmonics of 4 mrad full width half maximum (FWHM), the spot size at the grating is 1.3 mm. This is elongated to 4 mm by the grazing incidence angle of 19°. Thus 800 lines of the 200 lines/mm grating are illuminated, leading to a delay of $800 \times \lambda/c \approx 100\,\mathrm{fs}$, where the wavelength equals $\lambda = 34.4\,\mathrm{nm}$ and c is the speed of light. As the bandwidth $\Delta\lambda$ will always pass through the monochromator, the slit size sets the energy resolution but only little affects the pulse broadening (cf. Fig. 1).

The frequency shift across beam profile (spatial chirp) of a pulse diffracted off the grating leads to group velocity dispersion (GVD). This second order pulse broadening scales with $\lambda^3 \cdot N^2$ and is moderate in our setup (≈ 8 fs at $h\nu = 35.6$ eV)[42]. GVD likewise causes a frequency chirp of the pulse which we estimate to 30 meV over the 100 fs pulse duration at the sample position. The chirp leads to a small broadening of the ARPES spectra compared to the overall energy resolution of the experiment of about 200 meV. Note that this frequency shift cannot be time-resolved when probing initially occupied states.

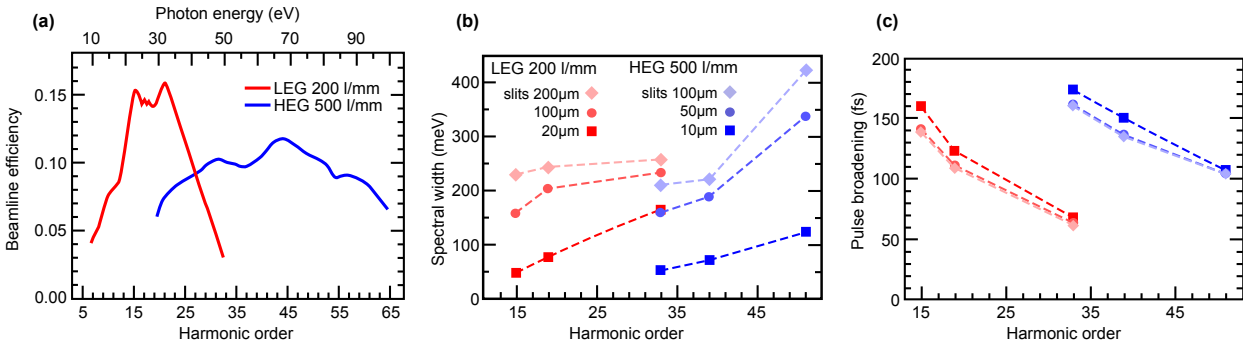

FIG. 1. Calculated performance of the monochromator beamline. (a) Beamline optical transmission (efficiency), which is dominated by the grating reflectivity. The lower scale gives the harmonic order in terms of the fundamental IR beam (800 nm), the corresponding photon energy is indicated on the upper scale. (b) Spectral width as a function of harmonic order for a range of slit widths and the appropriate grating. The plotted values include both the monochromator band pass and the inherent width of the respective harmonic. (c) Temporal broadening due to the grating shown for the same parameters as (b).

TABLE I. Optical parameters of the monochromating XUV beamline. All optical elements are toroidal and gold coated to a depth of 40 nm for optimal reflectivity.

optical element	mirrors	LEG	HEG
long radius	9567 mm	1000 mm	1000 mm
short radius	104.5 mm	104.9 mm	104.9 mm
deviation angle	168°	142°	142°
slope error rms [a]	≤ 2" / ≤ 5"	≤ 1" / ≤ 5"	≤ 1" / ≤ 5"
microroughness rms	≤ 0.5 nm	≤ 0.5 nm	≤ 0.5 nm
line density	-	200/mm	500/mm

[a] long axis / short axis

C. Beamline Realization

The layout of the beamline can be seen in Fig. 2, along with the other components forming the complete tr-ARPES experiment. Technical details of the XUV optics are presented in Table I.

The HHG process occurs in the gas cell. From there the XUV radiation co-propagates with the IR beam through two 2 mm diameter fixed apertures, which form a differential pumping stage between the gas cell chamber and the rest of the beamline. The apertures can also be used for coarse alignment and reduce the IR intensity. The rest of the IR radiation is blocked after the apertures by a 150 nm thick aluminium foil supported by a Ni mesh (Luxel Corp.) to protect the entrance slit of the monochromator and prevent the grating from heating. The measured transmission of the Al filter at 35.6 eV is about 50 % and rises with higher photon energies. It is mounted on a CF40 gate valve, which aids the differential pumping of the beamline and can be opened for alignment with the IR beam or a co-propagating HeNe laser beam. As Fig. 2 shows, after the Al filter, the XUV beam is focused at the entrance slit of the monochromator by a grazing-incidence toroidal mirror (Winlight). Located 1 m from the gas cell with a 500 mm focal length, the mirror relays a 1:1 image of the HHG source to the monochromator entrance slit. The monochromator grating relays an image of the entrance slit to the exit slit, and the second identical toroidal mirror images the monochromator exit slit onto the sample.

The monochromator itself is a customized Jobin-Yvon JY-VTM-EUV toroidal grating monochromator (entrance arm length 331 mm, exit arm length 320 mm) equipped with slits adjustable under vacuum for photon energy and bandwidth selection. The monochromator houses the two custom-made laminar toroidal gratings, which can be exchanged under vacuum.

Following the design of large grazing-incidence mirrors in synchrotron beamlines, we use a five-axis, six-strut arrangement with well proven reliability to support and adjust the two toroidal mirrors.[43] The chambers housing the optical elements are on heavy granite blocks, and mechanically decoupled from the surrounding beamline by bellows. Together with the computer controlled monochromator, this ensures easy and reliable user operation of the beamline. For alignment purpose and for assessment of the harmonic photon flux, two XUV sensitive photodiodes (AXUV100, International Radiation Detectors Inc.) can be introduced into the beamline before or after the monochromator (see Fig. 2)

The vacuum chambers housing the mirrors and gratings are each pumped with a vibrationally-isolated turbo-molecular pump (Pfeiffer, TMU 261P), leading to effective differential pumping along the beamline. Together with an ion-getter pump attached to the last chamber we reach ultra-high vacuum (UHV) conditions with a base pressure of

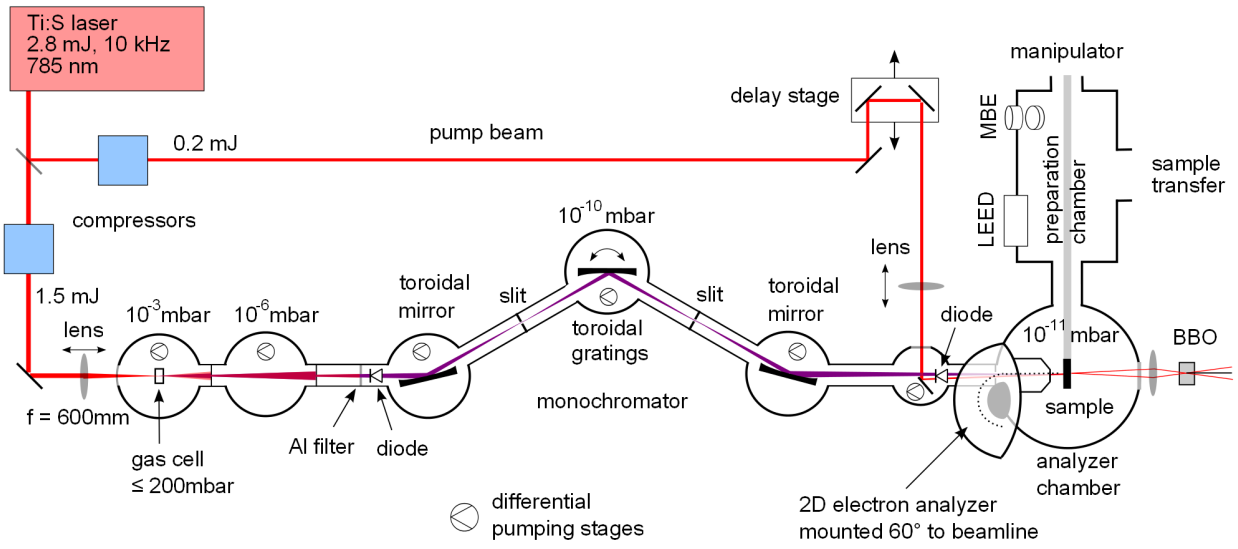

FIG. 2. Layout of the IR-pump – XUV-probe tr-ARPES experiment. Approximately 90 % of the Ti:S laser output is used for HHG, while the remaining 10 % is used for pumping the sample. Both beam paths have their own computer-controlled compressors for pulse duration control and a $\lambda/2-$plate + polarizer combination for power control. HHG occurs in the gas cell, typically in Ar. XUV sensitive photodiodes are located just after the Al filter and after the second toroidal mirror. The IR pump beam is introduced into the beamline after the second toroidal mirror. A BBO crystal behind the analyzer chamber is used to find the temporal overlap of the pump pulse and an IR pulse allowed to pass through the beamline.

10^{-10} mbar in the beamline and 10^{-11} mbar in the analyzer chamber.

D. The laser system

In order to minimize space charge effects due to electron-electron repulsion in photoemission from solid surfaces (see discussion below), it is desirable to release approximately one electron into the spectrometer with each probe pulse. This calls for a high repetition rate laser source. On the other hand, HHG is typically and most conveniently achieved with $> 500\,\mu$J pulses. This combination rapidly leads to high average power lasers. A reasonable compromise between repetition rate and pulse energy can be achieved with Titanium Sapphire (Ti:S) chirped-pulse amplifiers (CPA) running at 10 kHz and 1-2 mJ energy per pulse.

The laser chosen for our experiment is a commercial Ti:S CPA laser system (Red Dragon, Kapteyn Murnane Labs). The laser comprises a prism-compensated Ti:S oscillator running at 80 MHz followed by three helium-cooled multipass amplifier stages. Each stage is pumped at 532 nm by a 10 kHz Q-switched Nd:YAG laser (Photonics Industries, DM100-532) operating at 85 W. We have introduced a spatial filter (a 1:1 Newtonian telescope with a 200 μm diameter diamond pinhole at the focus) between the first and the second amplifier stage to avoid hot spots in the beam profile after the multipass amplifier. This incurs a power loss of $\approx 10\,\%$ but reliably avoids damage to the subsequent amplifier crystals. After two separate grating compressors in the pump and probe beam-paths with about 60 % transmission the laser delivers 17 W at 10 kHz (1.7 mJ/pulse) with a center wavelength of 785 nm and a pulse duration of 40 fs, as measured with frequency-resolved optical gating.

Approximately 10 % of the laser output is split off to excite (pump) the sample. It passes through a separate compressor, as shown in Fig. 2, allowing the pump pulse to be stretched to arbitrary durations without affecting the HHG process.

E. High-order Harmonic Generation

Since HHG is a highly nonlinear process, it is sensitively dependent on a number of experimental parameters. In addition to the laser wavelength, the pulse energy and duration, we must also optimize the beam profile, the focusing geometry, the interaction length and the gas pressure (and type).

To optimize focusing we tested different arrangements and found the best results using a lens with a focal length of 600 mm. The exact position of the focus is known to influence the harmonic generation efficiency through the Gouy phase,[44] and its optimum depends on the pump pulse intensity and the gas pressure. For our experiments the best results were achieved by positioning the focus just behind the gas cell in the beam propagation direction, towards the monochromator (at 1.5 mJ, 40 fs, and 100 mbar argon). It is noteworthy that any form of astigmatism in the IR focus at this point significantly reduces the harmonic yield.

The optimum length of the cell depends on the laser intensity and therefore on the focal length of the lens, the laser pulse energy, and pulse length. We have tested a number of different types of gas cells with an interaction length between 2 and 15 mm with walls of

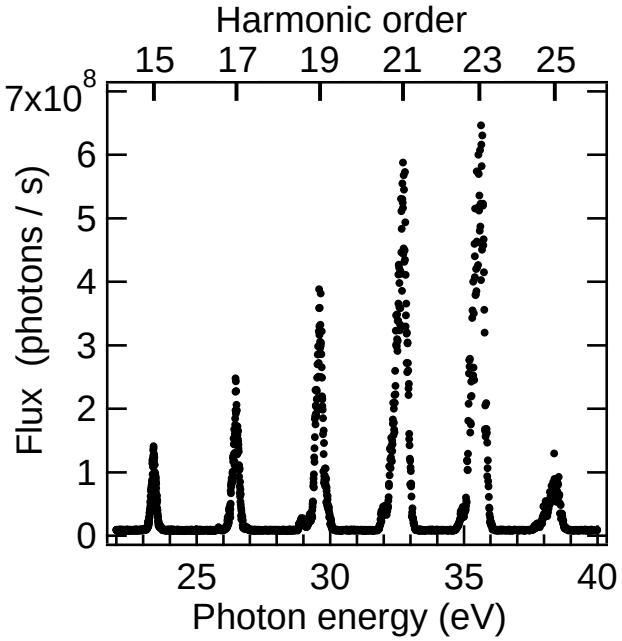

FIG. 3. A high-order harmonic spectrum generated in argon at 110 mbar by a 1.5 mJ, 40 fs pulse with a center wavelength of 785 nm. The spectrum was measured by recording the current from an XUV sensitive photodiode just before the sample position while scanning the monochromator grating. The slit size of the entrance and exit slits was adjusted for a monochromator resolution of 210 meV at harmonic 23. The FWHM bandwidth of harmonic 23 is 500 meV.

stainless steel and copper between $20 - 200\,\mu$m thick. The best was found to be a simple stainless steel tube ($\varnothing\, 3 \times 0.2\,$mm) with one end connected to the gas supply by compression fittings and the other flattened and folded over to seal it. The focused IR beam burns through the gas cell wall ensuring the holes have the correct diameter ($\approx 150\,\mu$m) and are perfectly aligned to the beam.

The argon pressure for the gas cell is computer controlled (MKS 640) and can reach up to 200 mbar. The tuneability of this pressure is important since it has a strong influence on the spectrum of the generated harmonics. Depending on the laser intensity we have found an Ar pressure of $50 - 100$ mbar to give the highest harmonic yield. During operation the pressure outside the cell stays below $5 \cdot 10^{-3}$ mbar, corresponding to a pressure gradient of about five orders of magnitude, due to the small holes in the cell walls. The gas cell chamber is pumped by a turbo-molecular pump (Pfeiffer TMU 512P 500 l/s) backed by a piston pump (Leybold Ecodry M15).

Many parameters of the beamline that must be optimized are controlled by a lab-written software: the gas cell pressure, the grating separation of both compressors (and therefore the IR pulse lengths), the power of the pump and HHG drive pulses and monochromator grating angle, *i.e.*, the XUV wavelength of the probe pulse. The pump and HHG drive IR pulses are characterized and optimized before each experiment using frequency-resolved optical gating. A typical XUV spectrum using the optimized parameters described above is shown in Fig. 3.

F. ARPES endstation

The endstation comprises three chambers separated by gate valves (see Fig. 2): A μ-metal analyzer chamber (VG Scienta), a sample preparation chamber and a sample garage.

The μ-metal chamber reduces the earth's magnetic field to values below 50 nT. It houses a hemispherical display-type photoelectron analyzer (Specs Phoibos 100) for ARPES. We use a peltier-cooled camera (PCO, sensicam qe) to monitor the count rates. This guarantees negligible thermal noise relative to the CCD readout noise, thus enabling measurements with exposure times of up to several minutes at each pump probe delay. To calibrate the count rate we operate the camera with a short exposure time and high readout repetition rate, which makes it possible to count single electrons. The analyzer chamber is pumped by an ion getter pump and a titanium sublimation pump, in addition to the turbomolecular pump on the preparation chamber. A further getter pump attached near the electron detector ensures low presssure throughout the analyzer. Together with the differential pumping along the beamline, these pumps allow a routine base pressure of 10^{-11} mbar, thus fulfilling the special vacuum conditions required for the study of bulk and surface electronic structures of reactive samples such as lanthanide metals.

The preparation chamber is designed for sample growth and characterization. It houses a LEED device, a sputter gun, a quadrupole mass spectrometer, a coil with an iron core to magnetize samples, gas inlets, a quartz balance for monitoring the sample growth and evaporators for molecular beam epitaxy. Attached to the preparation chamber is a differentially pumped double stage load-lock and sample garage. They facilitate quick sample exchange without breaking the vacuum in the main chambers.

A cryogenically coolable sample manipulator (Vab GmbH) carries two different samples

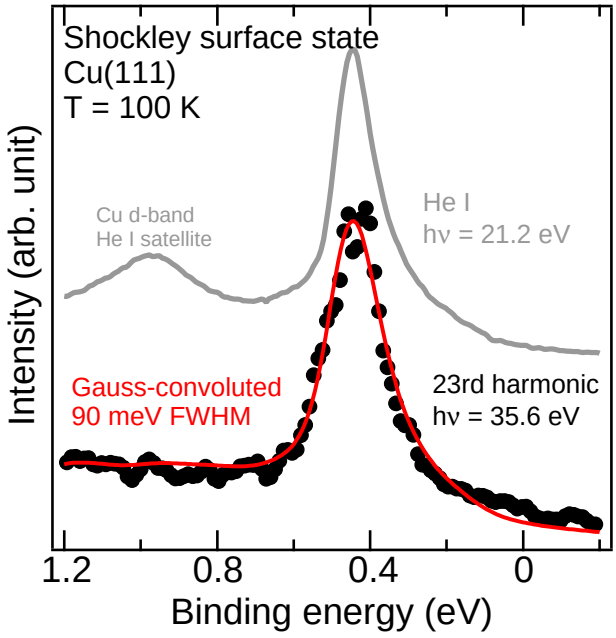

FIG. 4. Photoelectron spectra of the Cu(111) surface state at 100 K measured with the He I_α line at 21.2 eV photon energy (top) and with high-order harmonic radiation at 35.6 eV (bottom) with identical analyzer settings. The broad peak at $\approx$ 1.0 eV binding energy stems from the Cu d-band excited with the He-I satellite. The He I_α data is limited by the analyzer resolution. The solid red line is a convolution of these data with a Gaussian (with the satellite removed), which gives an energy bandwidth of 90 meV (FWHM) for the high-order harmonic radiation.

between the preparation and analyzer chambers on a copper extension built in-house. A fixed W(110) single crystal, as a substrate for the growth of thin-film samples such as Gd, and a holder for exchangeable samples. Both samples can be heated by electron bombardment. The tungsten crystal can be heated to 2100 K while its temperature is monitored by a type C thermocouple inserted into a small hole drilled in the side of the crystal. The temperature of the exchangeable sample is measured with a type K thermocouple. In addition the temperature of the whole manipulator head is monitored by type E thermocouple to prevent overheating of the copper parts when heating with a built-in Thermocoax heater.

G. ARPES: beamline energy resolution

We have performed a number of experiments specifically to test the performance of the beamline against its design specifications. Furthermore we have successfully performed experiments in the field of ultrafast magnetism for which the desired performance is simply a necessity. This section describes both of these experiments and their results to give a clear picture of our tr-ARPES experiment.

As stated above, the bandwidth of a single harmonic at a central energy of 35.6 eV generated by a 30-40 fs IR pulse is typically 500 meV. Since for a monochromator grating with a given line density and beam size the convolved widths of the entrance and exit slits determine the transmitted photon bandwidth, to reduce this to 150 meV the monochromator slits must be closed to typically 20 μm.

To measure the overall energy resolution of the experiment, we turn to the well known surface state of the Cu(111) surface. Following cycles of Ar^+ sputtering and annealing to prepare the Cu surface, we performed ARPES measurements using He I_α radiation from a discharge lamp and compared the results to ARPES with the 23rd harmonic ($h\nu = 35.6$ eV). The spectra in Fig. 4 were obtained by integrating the ARPES data over 0.1 Å^{-1} range of $k_\parallel$. Since the linewidth of radiation from the He lamp is a few meV, the observed linewidth of the surface state is dominated by the intrinsic resolution of the electron analyzer. For the data recorded with XUV from HHG the observed linewidth is then a convolution of the monochromator energy resolution (i.e. the XUV bandwidth) and the analyzer resolution. We are therefore able to use this measurement to establish the monochromator resolution for 10 μm slit size, which was found to be approximately 90 meV at 35.6 eV photon energy.

H. XUV photon flux

The XUV flux depends on many parameters of the HHG process, but for our experiments, where better energy resolution is desirable, the monochromator plays a dominant role. To achieve the resolution discussed above, we must forgo considerable flux. While this may appear to be a limitation, high fluxes lead to space-charge distortion of ARPES spectra (see discussion below). For the 23rd harmonic at 35.6 eV with the XUV photon bandwidth set to 150 meV, we typically have a flux of $3.6 \cdot 10^7$ photons/second reaching the sample.

This leads to approximately one electron *detected* per XUV probe pulse and space-charge distortion from the XUV can be neglected.

I. Time-resolved ARPES: time resolution

For time-resolved photoemission studies the spatial overlap of the pump and probe beams is beams is critical. To achieve this, we image the XUV and IR spots on a phosphor-coated plate in the exchangeable sample holder with a high resolution camera. This also allows the IR and XUV spot sizes to be measured.

Temporal overlap between the IR and XUV is achieved by crossing an attenuated IR beam that has traveled along the beamline with the attenuated pump beam in a β-barium-borate (BBO) crystal (see Fig. 2). To allow the fundamental to traverse the beamline, the Al filter is removed, and the monochromator grating set to zero order. Both pump and probe beams then pass through the analyzer chamber and out of a window, and are then focused into the BBO crystal at a small angle. The pump-probe delay is then scanned until a second harmonic signal from the crossed beams is observed spatially located between them. Even though the pump and probe beam paths are 10 m long after their separation, we could not observe jitter in the pump probe delay within the time resolution of 125 fs given by the XUV pulse length.

Having found the pump-probe spatial and temporal overlap we can perform tr-ARPES to evaluate the temporal resolution. Cut to 150 meV, the bandwidth at 35.6 eV would support a transform-limited pulse duration of approximately 12 fs FWHM, assuming a Gaussian spectrum. The broadening of the XUV pulse by the monochromator was calculated to be in the order of 100 fs, as discussed above and shown in Fig. 1 (c). To measure the actual XUV pulse duration, we performed a time-resolved ARPES measurement on the W(110) crystal in the geometry shown in Fig. 5 (a). The crystal was pumped by a *p*-polarized 50 fs IR pulse and probed with the XUV at 32.6 eV. In the proximity of the sample surface, outgoing photoelectrons excited by the XUV can exchange energy with the electric field of the IR pulse. The exchanged energy is a multiple of the IR photon energy, leading to the formation of sidebands in the photoelectron spectra.[45,46] The sideband amplitude as a function of time is shown in Fig. 5 (b), and represents a cross-correlation function between the IR and XUV pulses from which the XUV pulse duration can be recovered.[47] This measurement indicates

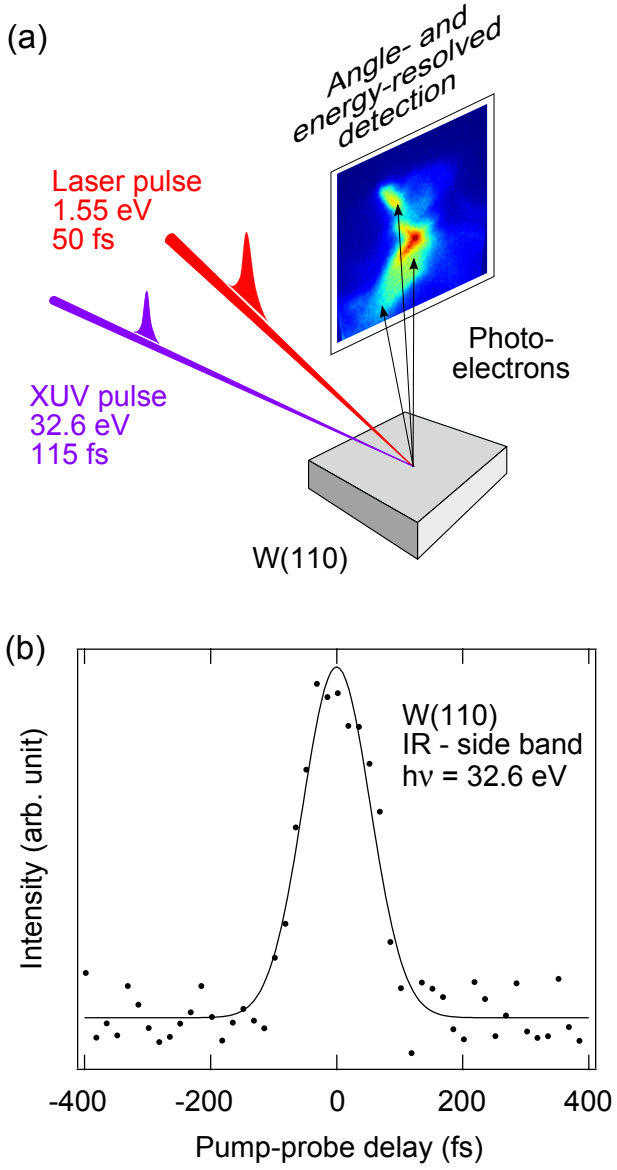

FIG. 5. (a) IR pump - XUV probe arrangement for tr-ARPES. The IR and XUV beams impinge on the sample with a small angle between them in the horizontal plane, which forms an angle of 60° to the surface normal. Photoelectrons are detected along the surface normal. (b) Cross-correlation measurement between 50fs IR and XUV at 32.6eV. The monochromator was set to 150 meV photon-energy resolution. The vertical axis shows the population of electrons lifted transiently above the Fermi level of the W(110) crystal by side-band formation. It gives a cross-correlation of the IR and XUV pulses, which is fitted to a Gaussian of FWHM 125 fs (solid red line). Deconvolution from the IR pulse yields an XUV pulse duration of ≈ 115 fs FWHM.

that our XUV pulse duration is approximately 100 fs, giving an overall time resolution for pump-probe experiments of 125 fs FWHM.

J. Time-resolved ARPES on Gd(0001)

To demonstrate the utility of tr-ARPES with high-order harmonic radiation we present ultrafast demagnetization data from a gadolinium thin film. If we are to meaningfully investigate the ultrafast magnetization dynamics of Gd, it is necessary to resolve the valence bands with sufficient energy and time resolution. Gd therefore presents an ideal testbed for our tr-ARPES experiment.

In addition, the nature of its magnetic ordering makes the Heisenberg ferromagnet gadolinium a model system in which to unravel equilibrium *vs.* non-equilibrium exchange interaction and spin dynamics. It has a half-filled $4f$ shell, leading to a large localized magnetic moment ($7\,\mu_B$) per atom. This is exchange-coupled to the $(5d6s)^3$ valence electrons and polarizes their spins, increasing the magnetic moment by a further $0.55\,\mu_B$ per atom. Magnetic ordering occurs because the valence electrons are itinerant and align the moments of adjacent atoms in an indirect exchange interaction explained by the Ruderman-Kittel-Kasuya-Yosida (RKKY) theory. Thus spin minority and majority components of the valence band are exchange split by an energy ΔE_{ex}. It is the transient behavior of these bands that we have observed following laser excitation.

Below its Curie temperature T_C of 293 K, Gd is ferromagnetic and can be driven towards the paramagnetic state by intense laser excitation.[48] Time-resolved studies have established that the $4f$ spins are coupled only weakly to the lattice,[49] giving a slow spin-lattice response-time of 40 ps.[17,48,50] Thus laser excitation of the valence bands provides a fast spin excitation channel decoupled from slow 4f spin-lattice effects.[51]

To prepare single-crystalline samples for ARPES, 10 nm thick Gd(0001) films were grown epitaxially on the W(110) crystal at room temperature and a pressure of 10^{-10} mbar. The deposition rate was monitored with a quartz balance and kept to 0.1 Å/second. The film was then annealed to 650 K and finally cooled with liquid nitrogen to approximately 90 K. The photoemission experiment was conducted at a pressure of 3×10^{-11} mbar.

Tr-ARPES measurements were performed on this film by exciting the sample with the IR pulse and probing the band structure with the XUV pulse in the geometry shown in Fig.

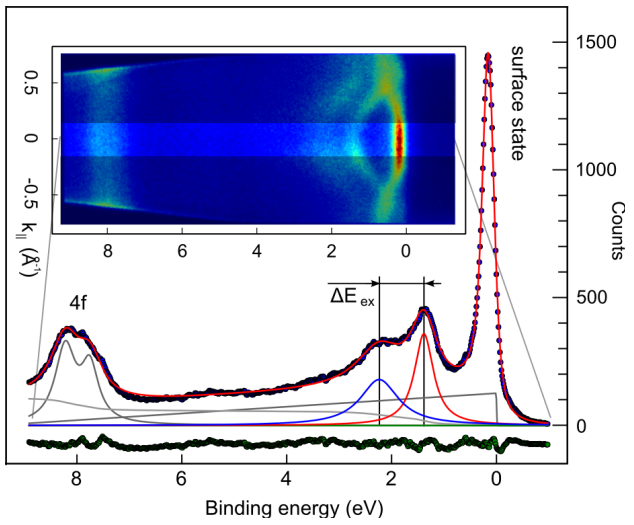

FIG. 6. Photoemission spectrum from a 10 nm thick Gd(0001) film on a W(110) substrate. The inset shows an ARPES image recorded for five minutes at one pump-probe delay using the 23rd harmonic at 35.6 eV. A photoelectron spectrum (blue points) is extracted by integrating over the highlighted stripe around $k_{\|} = 0$. This is then repeated for all pump-probe delays. The energy bandwidth of the XUV was 150 meV. The electron analyzer set to wide angle mode ($\pm 13°$ acceptance angle) at a pass energy of 60 eV and an entrance-slit width of 0.5 mm has a calculated energy resolution of 150 meV FWHM. The upper limit of the total energy resolution is given by the 260 meV FWHM of the Gd surface state. The individual components used to fit the data (solid lines) are explained in the text.

5 (a). The pump beam was focused to a spot of 1 mm (FWHM) in diameter on the sample, yielding an absorbed fluence of 1.2 mJ cm^{-2}. To ensure excitation only in the plane of the Gd surface and thus reduce the number of photoelectrons emitted directly by the pump pulse, the beam was *s*-polarized. After preliminary data nevertheless showed pump-induced space charge distortion of the spectra, a topic discussed in detail below, the pump pulse duration was stretched to 300 fs. Of course this reduced the experimental time resolution to around 300 fs, however this was still sufficient to capture the dynamics of the Gd valence band, as we show below.

A tr-ARPES experiment is conducted by collecting an image at each pump-probe delay for 30 s, and then repeating the measurement several times. In this way any slow fluctuations in the laser or XUV pointing or power, or slow degradation of the sample affect all pump-

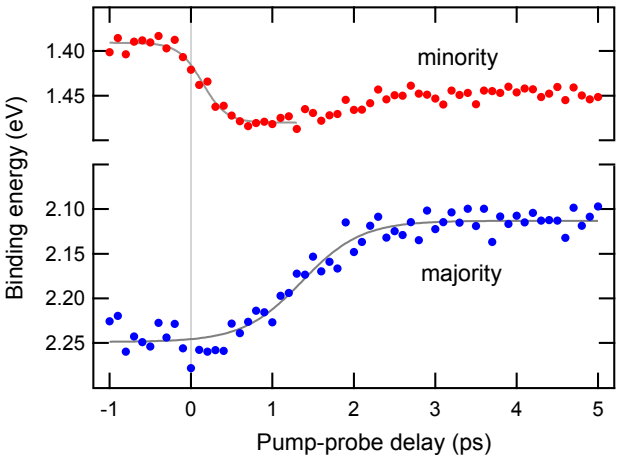

FIG. 7. Temporal evolution of the valence band minority and majority component in Gadolinium upon excitation with an s-polarized IR pulse stretched to 300 fs duration, delivering an absorbed IR fluence of 1.2 mJ cm^{-2}. The binding energies were extracted from the tr-ARPES data and fitted as shown in Fig. 6. The solid curves are fits to sigmoid functions serving to highlight the different dynamics of the two spin components, namely a significant delay between the onset of the majority response compared to that of the minority. The recording time of the complete data set was 5 hours.

probe data relatively evenly. The inset to Fig. 6 shows one such raw ARPES image taken at a pump-probe delay of -1 ps (IR pulse arriving 1 ps after the XUV probe pulse). With an XUV bandwidth of 150 meV and the electron analyzer in wide angle mode ($\pm 13^\circ$ acceptance angle) with a pass energy of 60 eV and an entrance slit width of 0.5 mm, this image took 5 minutes to record (10 repetitions of 30 s). These settings reduce the energy resolution significantly compared to the ultimate values discussed above. It could be improved at the cost of count rate by choosing a smaller entrance slit of the analyzer, changing the lens mode for a smaller acceptance angle and reducing the pass energy. If these settings are needed for comparing spectral features spread over a wide range of energies and points in k-space, as in our case the Gd 4f state at about 8 eV binding energy and the surface state at the Fermi edge together with the dispersion of the valence band, then the limiting factor is the size of the analyzer hemispheres together with the analyzer entrance slit width.

A photoelectron spectrum is extracted from the ARPES image by integrating over a small range of $k_\parallel$ around the Γ point, as indicated by the highlighted strip in the figure. The resulting spectrum is then fitted by 5 Lorentzians representing the surface state, the

$4f$ level (bulk and surface component) and the majority (blue) and minority (red) spin components of the valence band. A linear background accounts for elastic electron scattering from degenerate points in the Brillouin zone and the bulk states contribute to a Shirley background[52]. The Shirley background is assumed to be proportional to the area of the peak above the background to lower binding energies. Best fit results were obtained by convolving the spectra with a 210 meV instrument function to model the energy resolution. The width of the Gd surface state of 260 meV (FWHM) sets an upper limit to the overall energy resolution of the photoemission experiment. The minority (blue) and majority (red) spin components of the exchange split valence band are found initially at 1.39 and 2.25 eV binding energy, respectively. These values are in excellent agreement with synchrotron measurements.[53] The exchange splitting ΔE_{ex} is the difference in binding energy of the the two valence band components. Of particular interest is the collapse of this exchange splitting, because, at least under thermal equilibrium conditions, it can be used as a direct measure of the sample magnetization. Therefore spectra are decomposed as described above for every pump-probe delay. Evidently, our experiment has sufficient energy resolution that these peaks can be distinguished from each other by the fitting routine. Fig. 7 shows that indeed this was possible, allowing us to independently monitor the binding energies of the two bands for all pump-probe delays. Crucially this data shows different dynamical behavior in the minority and majority bands, which had not been observed previously or predicted theoretically[51].

The data above were recorded with the IR pump pulse stretched to $\approx$ 300 fs to reduce space-charge distortion (see below) without losing temporal resolution of the key changes in the spectra. When the IR pulse was compressed to $\approx$ 50 fs and the sample warmed to 210 K, we observe that the minority band reacts within the experimental time resolution. This measurement, shown in Fig. 8, offers another measurement of the cross-correlation between the XUV and the IR, confirming the value shown in Fig. 5.

K. Space-charge effects in tr-ARPES

Space-charge distortion of ARPES spectra occurs when a cloud of low-energy electrons is formed at the sample surface, either through secondary electron generation by high energy electrons excited by an XUV photon, or by electrons lifted just above the vacuum level by a

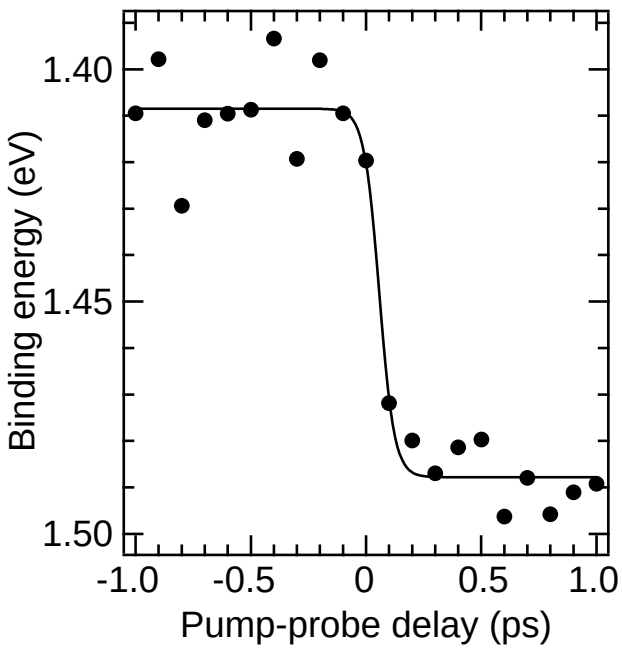

FIG. 8. Temporal evolution of the spin minority component of the valence band of Gd(0001) upon excitation with an *s*-polarized 50 fs IR pulse. The band position was fitted as shown in Fig. 6. Deconvolution of the decay time of this curve from the IR pulse duration yields an XUV pulse duration of ≤ 100 fs, confirming the sideband measurement.

lower energy photon. Outgoing photoelectrons experience acceleration by the electric field of this cloud that is dependent on their emission time and energy. This leads to energetic shifting and broadening of the photoemission spectral features and is thus a severe restriction for measurements with already moderate resolution. Space-charge is known to be a problem in time-resolved photoemission studies from solid surfaces, especially for experiments with high pulse energies (typically at low repetition rates).[46,54,55]

We observe space-charge effects in our experiment from both the IR and XUV excitation, and both can significantly distort the spectra. Fig. 9 (a) shows the effects of space-charge generated by photoelectrons excited by the XUV pulse. The data are extracted from changes in the width and energetic position of the surface state (Fig. 6) as a function of the XUV flux. XUV space-charge effects become observable when the flux from the monochromator is higher than $\approx 10^4$ photons/pulse ($h\nu = 35.6$ eV), so at the XUV fluences we measure with, the space-charge effects can be neglected. As Fig. 9 confirms, XUV space-charge distortions are approximately linear over a wide fluence range.[54] At a flux of about 10^5 photons/pulse

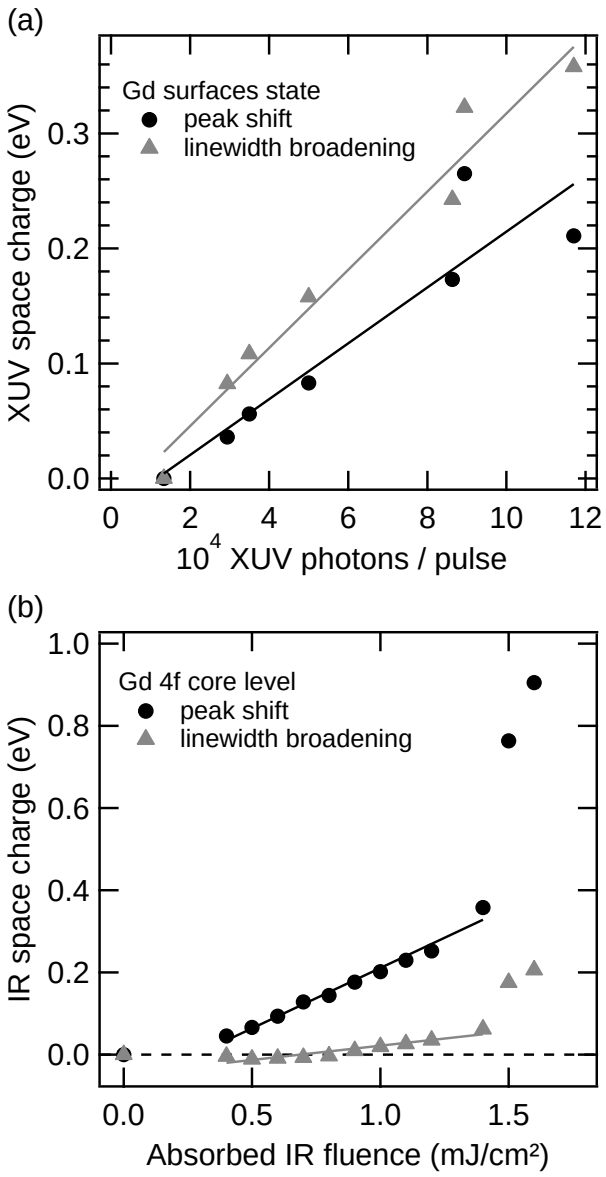

FIG. 9. Space-charge shift (circles) and broadening (triangles) of the spectra as measured from changes to the Gd(0001) surface state and the Gd 4f core level. a) shows the probe pulse space charge of the harmonic radiation. b) the pump-probe delay dependent contribution of the IR pump pulse, here at 4 ps pump-probe delay where it reaches a maximum.

the XUV induced space charge shifts the spectrum by 200 meV, and is accompanied by a decline of the energy resolution by an additional 300 meV FWHM. Broadening of the spectra by XUV space-charge comprises two effects: acceleration of the outgoing electron and pulse-to-pulse fluctuations in the HHG process. The latter broadens the spectrum

further due to integration over spectra that have experienced different energy shifts. It is for this reason that the broadening in Fig. 9 (a) is larger than the energetic shift, in contrast to the equivalent results for IR-induced space-charge distortions, which are discussed next.

Space-charge distortion from electrons excited by the IR pump pulse is more complicated because it is delay-dependent. In dynamical spectra its compensation requires a spectral feature that does by its nature not move. In our Gd(0001) measurements the $4f$ level, with a binding energy of 8 eV, cannot be excited by the IR pump pulse. Furthermore, we measured the binding energy of this level as a function of temperature using He I_α radiation and found it to show no significant shift (≤ 5 meV in the temperature range of $100-300$ K). Thus we can use any observed temporal shift of the $4f$ level to correct for the IR-induced space-charge distortion. Its extent is summarized in Fig. 9 (b) as a function of absorbed fluence. At low fluences we see a linear increase in the peak shift and a small linewidth broadening with a sudden rapid increase at about 1.5 mJ/cm^2. To excite an electron from the Fermi energy to the vacuum level requires, for Gd with a preparation-dependent work function of $3.0-3.7$ eV, at least two 1.5 eV photons, so this curve can be interpreted as a non-linear increase in multi-photon absorbtion.

With knowledge of the IR-induced distortion, we correct all time-dependent spectral shifts to those of the $4f$ level to eliminate energetic shifts. We can therefore be certain that space-charge effects are not responsible for the dynamics observed in Fig. 7. However, since two-photon absorption scales with the *intensity*, these findings put an upper limit on the IR intensity we can employ to demagnetize the sample if we are to retain sufficient energy resolution. Thus a balance must also be struck between time resolution and pump pulse energy (fluence): a shorter pulse with less energy or a longer one with more.

L. Conclusion

We have described the design, construction and operation of a novel monochromated tr-ARPES experiment. Its experimental realization matches the calculated performance well. The experiment exploits the femtosecond time resolution of XUV pulses from high-order harmonic sources without sacrificing the energy resolution necessary to capture interesting details of the band structure. This makes high-order harmonic radiation a powerful source for the investigation of band dynamics in solids. Tr-ARPES studies based on HHG will give

new insights into the physics of correlated electron materials. XUV space-charge effects will make it favorable to design HHG sources with a repetition rate even higher than 10 kHz. Elevated repetition rates will make it possible to combine spin-, time- and angle-resolved photoemission in future experiments.

We gratefully acknowledge funding by the Deutsche Forschungsgemeinschaft through grant WE2037/4-1, by the Leibniz graduate school *Dynamics in New Light* and by the Helmholtz Virtual Institute *Dynamic Pathways in Multidimensional Landscapes*.

REFERENCES

[1]F. Reinert and S. Hüfner, New J. Phys. **7**, 97 (2005).

[2]A. Bostwick, T. Ohta, T. Seyller, K. Horn, and E. Rotenberg, Nature Phys. **3**, 36 (2006).

[3]A. Hofmann, X. Y. Cui, J. Schäfer, S. Meyer, P. Höpfner, C. Blumenstein, M. Paul, L. Patthey, E. Rotenberg, J. Bünemann, F. Gebhard, T. Ohm, W. Weber, and R. Claessen, Phys. Rev. Lett. **102**, 187204 (2009).

[4]M. Hoesch, T. Greber, V. Petrov, M. Muntwiler, M. Hengsberger, W. Auwärter, and J. Osterwalder, J. Electron. Spectrosc. Relat. Phenom. **124**, 263 (2002).

[5]C. Tusche, M. Ellguth, A. A. Ünal, C.-T. Chiang, A. Winkelmann, A. Krasyuk, M. Hahn, G. Schönhense, and J. Kirschner, Appl. Phys. Lett. **99**, 032505 (2011).

[6]J. Sánchez-Barriga, J. Fink, V. Boni, I. Di Marco, J. Braun, J. Minár, A. Varykhalov, O. Rader, V. Bellini, F. Manghi, H. Ebert, M. I. Katsnelson, A. I. Lichtenstein, O. Eriksson, W. Eberhardt, and H. A. Dürr, Phys. Rev. Lett. **103**, 267203 (2009).

[7]R. Haight, Surf. Sci. Rep. **21**, 275 (1995).

[8]H. Petek and S. Ogawa, Prog. Surf. Sci. **56**, 239 (1997).

[9]K. Döbrich, A. Bostwick, J. L. McChesney, K. Rossnagel, E. Rotenberg, and G. Kaindl, Phys. Rev. Lett. **104**, 246401 (2010).

[10]R. Cortés, L. Rettig, Y. Yoshida, H. Eisaki, M. Wolf, and U. Bovensiepen, Phys. Rev. Lett. **107**, 097002 (2011).

[11]F. Schmitt, P. S. Kirchmann, U. Bovensiepen, R. G. Moore, L. Rettig, M. Krenz, J.-H. Chu, N. Ru, L. Perfetti, D. H. Lu, M. Wolf, I. R. Fisher, and Z.-X. Shen, Science **321**, 1649 (2008).

[12]J. A. Sobota, S. Yang, J. G. Analytis, Y. L. Chen, I. R. Fisher, P. S. Kirchmann, and Z.-X. Shen, Phys. Rev. Lett. **108**, 117403 (2012).

[13]S. Danzenbächer, D. V. Vyalikh, K. Kummer, C. Krellner, M. Holder, M. Höppner, Y. Kucherenko, C. Geibel, M. Shi, L. Patthey, S. L. Molodtsov, and C. Laubschat, Phys. Rev. Lett. **107**, 267601 (2011).

[14]A. Pietzsch, A. Föhlisch, M. Beye, M. Deppe, F. Hennies, M. Nagasono, E. Suljoti, W. Wurth, C. Gahl, K. Döbrich, and A. Melnikov, New J. Phys. **10**, 033004 (2008).

[15]K. Holldack, T. Kachel, S. Khan, R. Mitzner, and T. Quast, Phys. Rev. ST Accel. Beams **8**, 040704 (2005).

[16]C. Stamm, N. Pontius, T. Kachel, M. Wietstruk, and H. A. Dürr, Phys. Rev. B **81**, 104425 (2010).

[17]M. Wietstruk, A. Melnikov, C. Stamm, T. Kachel, N. Pontius, M. Sultan, C. Gahl, M. Weinelt, H. A. Dürr, and U. Bovensiepen, Phys. Rev. Lett. **106**, 127401 (2011).

[18]R. W. Schoenlein, S. Chattopadhyay, H. H. W. Chong, T. E. Glover, P. A. Heimann, C. V. Shank, A. A. Zholents, and M. S. Zolotorev, Science **287**, 2237 (2000).

[19]A. Melzer, D. Kampa, J. Wang, and T. Fauster, Phys. Rev. B **80**, 205424 (2009).

[20]M. Bauer, J. Phys. D: Appl. Phys. **38**, R253 (2005).

[21]F. Frassetto, S. Bonora, P. Villoresi, L. Poletto, E. Springate, C. A. Froud, I. C. E. Turcu, A. J. Langley, D. S. Wolff, J. L. Collier, S. S. Dhesi, and A. Cavalleri, Proc. of SPIE **7077**, 707713 (2008).

[22]A. L. Cavalieri, N. Müller, T. Uphues, V. S. Yakovlev, A. Baltuska, B. Horvath, B. Schmidt, L. Blümel, R. Holzwarth, S. Hendel, M. Drescher, U. Kleineberg, P. M. Echenique, R. Kienberger, F. Krausz, and U. Heinzmann, Nature **449**, 1029 (2007).

[23]C.-T. Chiang, A. Blättermann, M. Huth, J. Kirschner, and W. Widdra, Appl. Phys. Lett. **101**, 071116 (2012).

[24]P. B. Corkum, Phys. Rev. Lett. **71**, 1994 (1993).

[25]F. Krausz and M. Ivanov, Rev. Mod. Phys. **81**, 163 (2009).

[26]C. La-O-Vorakiat, M. Siemens, M. M. Murnane, H. C. Kapteyn, S. Mathias, M. Aeschlimann, P. Grychtol, R. Adam, C. M. Schneider, J. M. Shaw, H. Nembach, and T. J. Silva, Phys. Rev. Lett. **103**, 257402 (2009).

[27]R. Sandberg, D. Raymondson, C. La-O-Vorakiat, A. Paul, K. Raines, J. Miao, M. Murnane, H. Kapteyn, and W. Schlotter, Opt. Lett. **34**, 1618 (2009).

[28]E. Magerl, S. Neppl, A. L. Cavalieri, E. M. Bothschafter, M. Stanislawski, T. Uphues, M. Hofstetter, U. Kleineberg, J. V. Barth, D. Menzel, D. F. Krausz, R. Ernstorfer, R. Kienberger, and P. Feulner, Rev. Sci. Instrum. **82**, 063104 (2011).

[29]G. L. Dakovski, Y. Li, T. Durakiewicz, and G. Rodriguez, Rev. Sci. Instrum. **81**, 073108 (2010).

[30]S. Mathias, L. Miaja-Avila, M. M. Murnane, H. Kapteyn, M. Aeschlimann, and M. Bauer, Rev. Sci. Instrum. **78**, 083105 (2007).

[31]J. C. Petersen, S. Kaiser, N. Dean, A. Simoncig, H. Y. Liu, A. L. Cavalieri, C. Cacho, I. C. E. Turcu, E. Springate, F. Frassetto, L. Poletto, S. S. Dhesi, H. Berger, and A. Cavalleri, Phys. Rev. Lett. **107**, 177402 (2011).

[32]P. Wernet, J. Gaudin, K. Godehusen, O. Schwarzkopf, and W. Eberhardt, Rev. Sci. Instrum. **82**, 063114 (2011).

[33]J. Norin, K. Osvay, F. Albert, D. Descamps, J. Yang, A. Lhuillier, and C.-G. Wahlström, Appl. Opt. **43**, 1072 (2004).

[34]L. Nugent-Glandorf, M. Scheer, D. A. Samuels, V. Bierbaum, and S. R. Leone, Rev. Sci. Instrum. **73**, 1875 (2002).

[35]L. Poletto, Appl. Phys. B **78**, 1013 (2004).

[36]P. Siffalovic, M. Drescher, M. Spieweck, T. Wiesenthal, Y. C. Lim, R. Weidner, A. Elizarov, and U. Heinzmann, Rev. Sci. Instrum. **72**, 30 (2001).

[37]T. Haarlammert and H. Zacharias, Curr. Opin. Solid State Mater. Sci. **13**, 13 (2009).

[38]F. Schäfers and M. Krumrey, "Reflec, program to calculate vuv/x-ray optical elements and synchrotron radiation beamlines," Tech. Rep. TB 201/96 (Berliner Elektronen Speicherring für Synchrotronstrahlung, 1996).

[39]F. Schäfers, in *Modern Developments in X-Ray and Neutron Optics*, Springer Series in optical science, Vol. 137, edited by A. Erko, M. Idir, T. Krist, and A. G. Michette (Springer Berlin Heidelberg, 2008) pp. 9–41.

[40]P. Wernet, K. Godehusen, O. Schwarzkopf, and W. Eberhardt, in *Ultrafast Phenomena XV*, Springer Series in Chemical Physics, Vol. 88, edited by P. Corkum, D. M. Jonas, R. J. D. Miller, and A. M. Weiner (Springer Berlin Heidelberg, 2007) pp. 45–47.

[41]L. Nugent-Glandorf, M. Scheer, M. Krishnamurthy, J. Odom, and S. Leone, Phys. Rev. A **62**, 023812 (2000).

[42]O. E. Martinez, Optics Comm. **59**, 229 (1986).

[43]T. Noll, T. Zeschke, G. Reichardt, H. Lammert, and W. Gudat, Nucl. Instrum. Methods Phys. Res., Sect. A **467-468**, 775 (2001).

[44]P. Salières, A. L'Huillier, and M. Lewenstein, Phys. Rev. Lett. **74**, 3776 (1995).

[45]L. Miaja-Avila, C. Lei, M. Aeschlimann, J. Gland, M. Murnane, H. Kapteyn, and G. Saathoff, Phys. Rev. Lett. **97**, 113604 (2006).

[46]G. Saathoff, L. Miaja-Avila, M. Aeschlimann, M. Murnane, and H. Kapteyn, Phys. Rev. A **77**, 022903 (2008).

[47]J. M. Schins, P. Breger, P. Agostini, R. C. Constantinescu, H. G. Muller, A. Bouhal, G. Grillon, A. Antonetti, and A. Mysyrowicz, J. Opt. Soc. Am. B: Opt. Phys. **13**, 197 (1996).

[48]A. Vaterlaus, T. Beutler, and F. Meier, Phys. Rev. Lett. **67**, 3314 (1991).

[49]S. Abdelouahed and M. Alouani, Phys. Rev. B **79**, 054406 (2009).

[50]A. Melnikov, H. Prima-Garcia, M. Lisowski, T. Gießel, R. Weber, R. Schmidt, C. Gahl, N. Bulgakova, U. Bovensiepen, and M. Weinelt, Phys. Rev. Lett. **100**, 107202 (2008).

[51]R. Carley, K. Döbrich, B. Frietsch, C. Gahl, M. Teichmann, O. Schwarzkopf, P. Wernet, and M. Weinelt, Phys. Rev. Lett. **109**, 057401 (2012).

[52]D. A. Shirley, Phys. Rev. **5**, 4709 (1972).

[53]C. Schüßler-Langeheine, *Magnetic Properties of Thin Films of Heavy Lanthanide Metals Studied by Magnetic X-Ray Diffraction and High-Resolution Photoemission.*, Ph.D. thesis, Fachbereich Physik, Freie Universität Berlin (1999).

[54]S. Hellmann, K. Rossnagel, M. Marczynski-Bühlow, and L. Kipp, Phys. Rev. B **79**, 035402 (2009).

[55]S. Passlack, S. Mathias, O. Andreyev, D. Mittnacht, M. Aeschlimann, and M. Bauer, J. Appl. Phys. **100**, 024912 (2006).

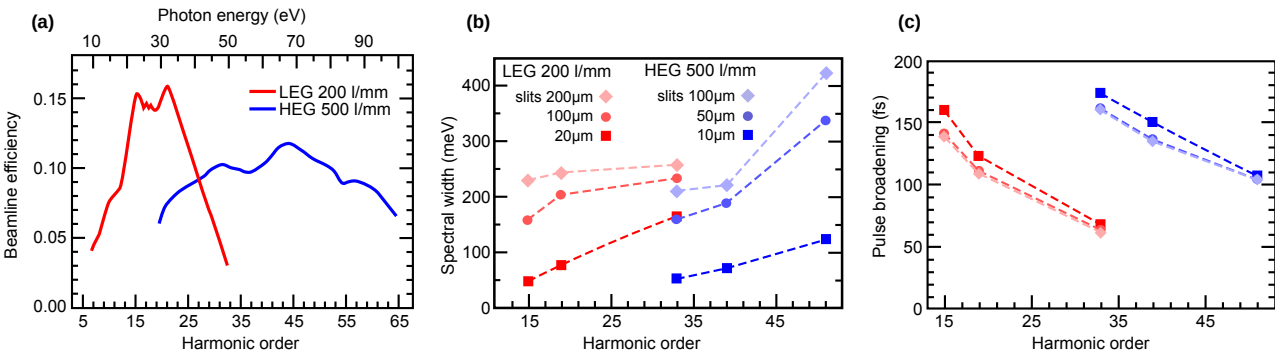
(a)
Photon energy (eV)
10
30
50
70
90
LEG 200 l/mm
HEG 500 l/mm
Beamline efficiency
0.15
0.10
0.05
0.00
5
15
25
35
45
55
65
Harmonic order
(b)
LEG 200 l/mm
HEG 500 l/mm
slits 200µm
100µm
20µm
slits 100µm
50µm
10µm
Spectral width (meV)
400
300
200
100
0
15
25
35
45
Harmonic order
(c)
Pulse broadening (fs)
200
150
100
50
0
15
25
35
45
Harmonic order

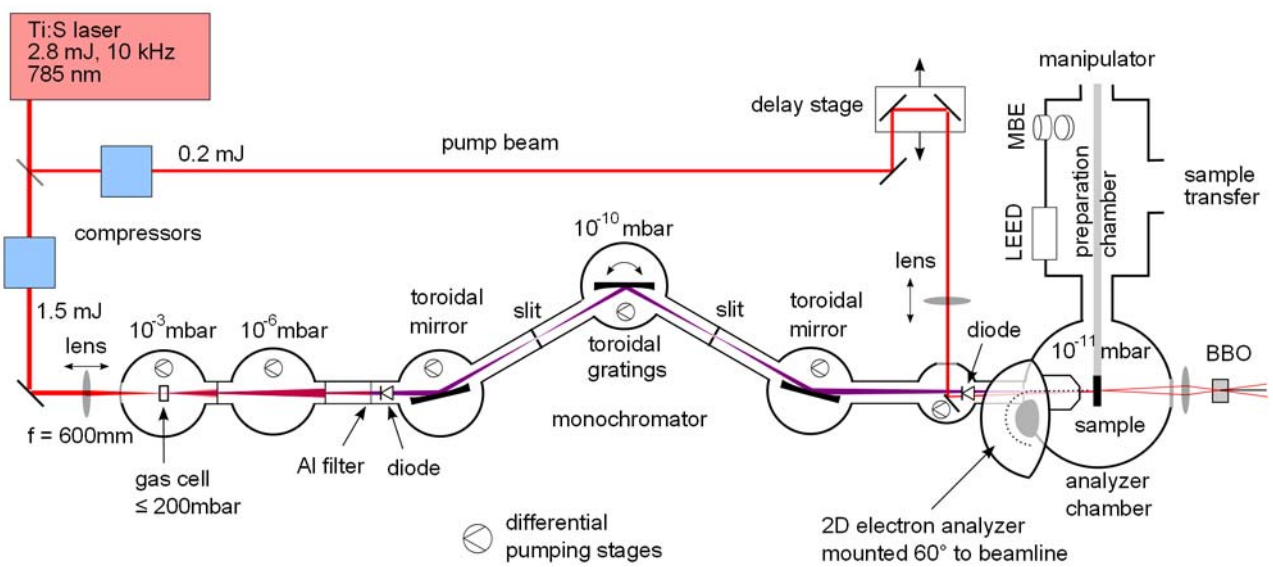
Ti:S laser
2.8 mJ, 10 kHz
785 nm
0.2 mJ
pump beam
delay stage
manipulator
MBE
LEED
preparation chamber
sample transfer
compressors
1.5 mJ
lens
f = 600mm
10-3 mbar
10-6 mbar
gas cell
≤ 200mbar
Al filter
diode
toroidal mirror
slit
10-10 mbar
toroidal gratings
monochromator
slit
toroidal mirror
lens
diode
10-11 mbar
sample
analyzer chamber
BBO
differential pumping stages
2D electron analyzer mounted 60° to beamline

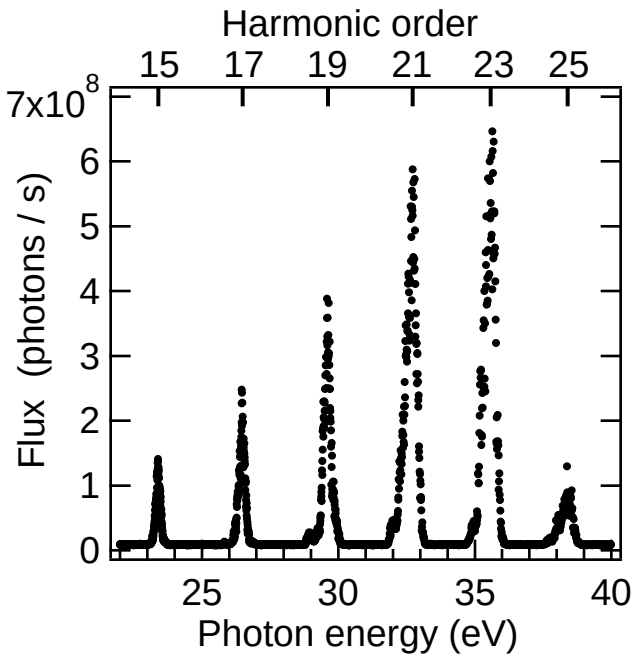
Harmonic order
15
17
19
21
23
25
7x10^8
6
5
4
3
2
1
0
Flux (photons / s)
25
30
35
40
Photon energy (eV)

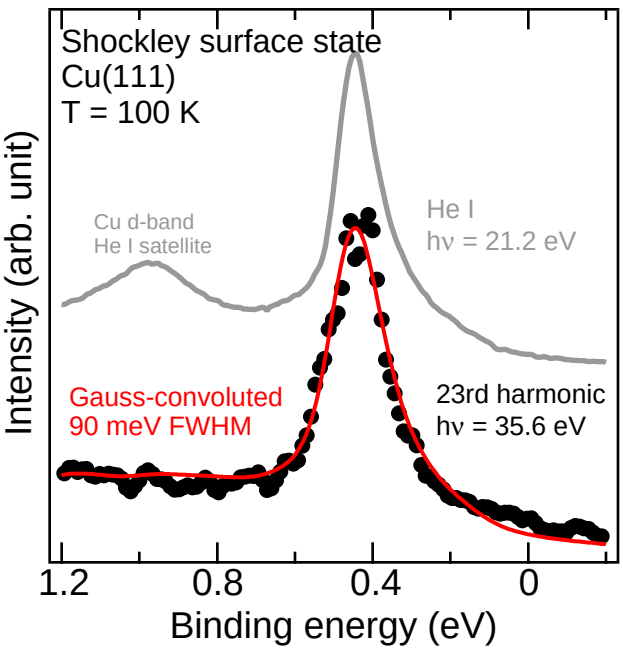
Shockley surface state
Cu(111)
T = 100 K
Cu d-band
He I satellite
He I
hν = 21.2 eV
Gauss-convoluted
90 meV FWHM
23rd harmonic
hν = 35.6 eV
Intensity (arb. unit)
1.2
0.8
0.4
0
Binding energy (eV)

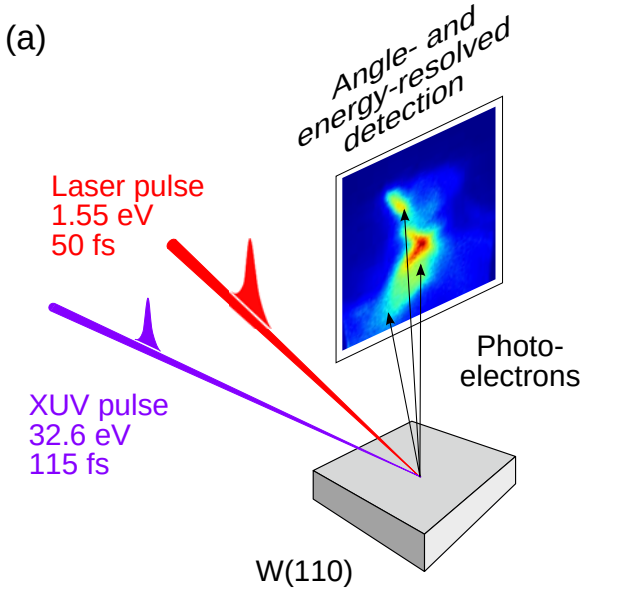
(a)
Angle- and
energy-resolved
detection
Laser pulse
1.55 eV
50 fs
XUV pulse
32.6 eV
115 fs
Photo-
electrons
W(110)

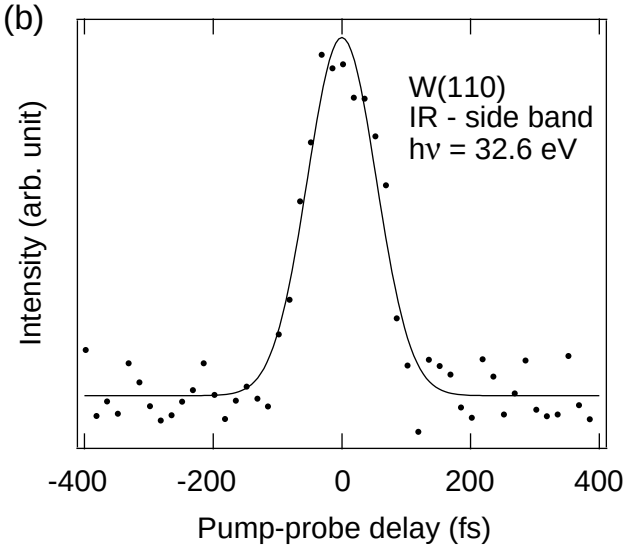
(b)
W(110)
IR - side band
hν = 32.6 eV
Intensity (arb. unit)
-400
-200
0
200
400
Pump-probe delay (fs)

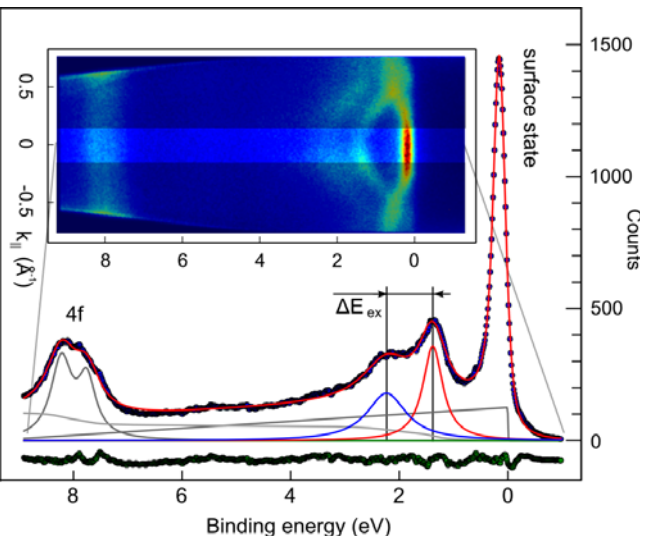
surface state
1500
1000
500
0
Counts
0.5
0
-0.5
$k_{||}$ (Å^{-1})
8
6
4
2
0
4f
ΔE_{ex}
Binding energy (eV)

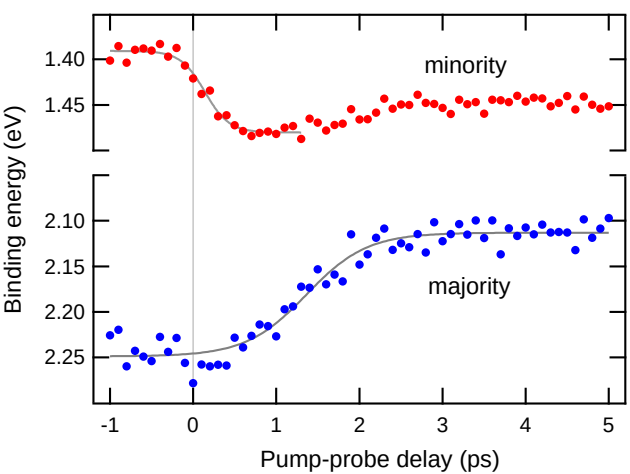
minority
majority
1.40
1.45
2.10
2.15
2.20
2.25
-1
0
1
2
3
4
5
Binding energy (eV)
Pump-probe delay (ps)

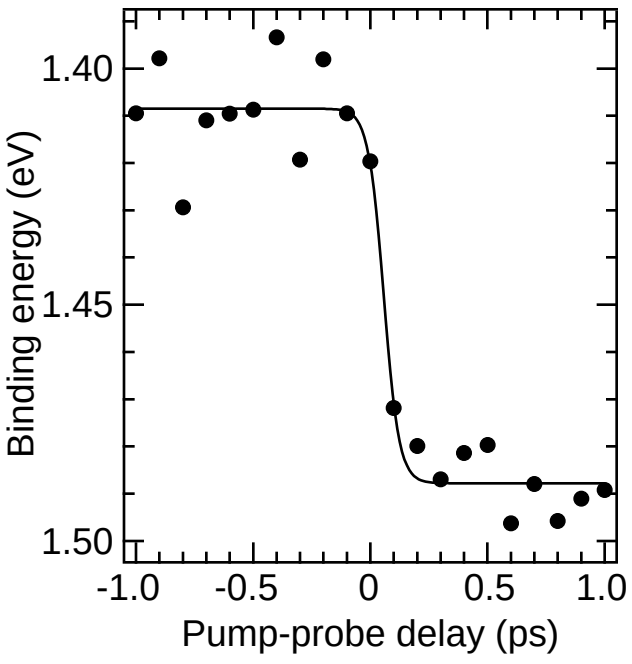
1.40
1.45
1.50
Binding energy (eV)
-1.0
-0.5
0
0.5
1.0
Pump-probe delay (ps)

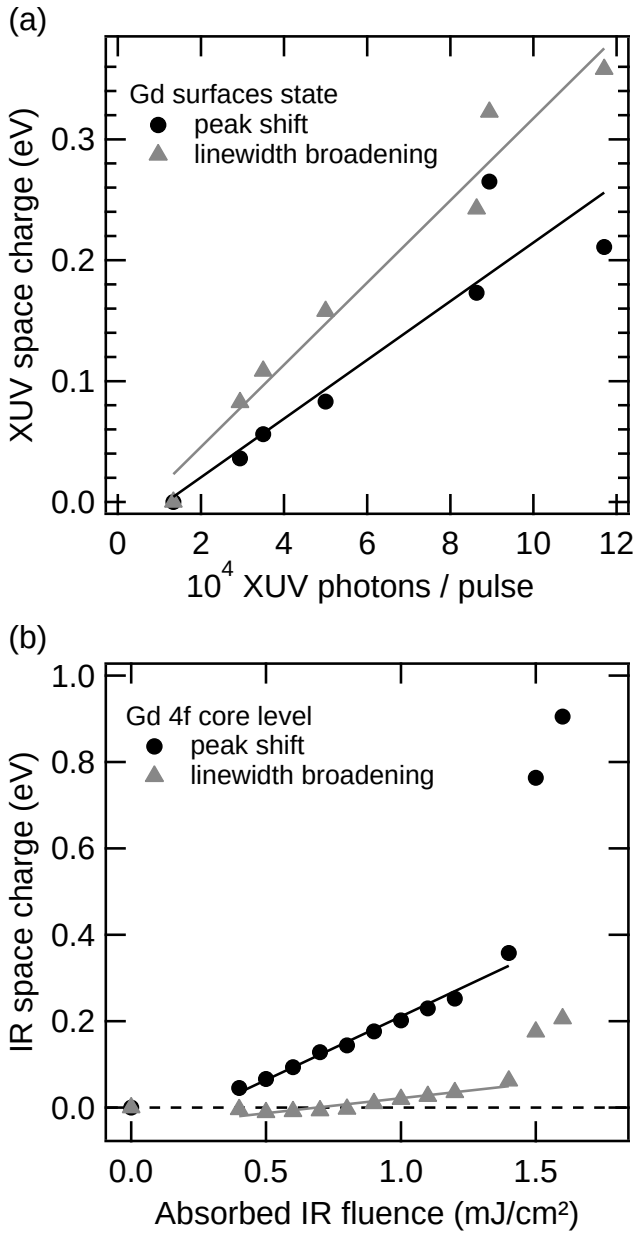
(a)
Gd surfaces state
peak shift
linewidth broadening
XUV space charge (eV)
0.0
0.1
0.2
0.3
0
2
4
6
8
10
12
10^4 XUV photons / pulse
(b)
Gd 4f core level
peak shift
linewidth broadening
IR space charge (eV)
0.0
0.2
0.4
0.6
0.8
1.0
0.0
0.5
1.0
1.5
Absorbed IR fluence (mJ/cm²)